Design and *In Vivo* Verification of a CMOS Bone-Guided Cochlear Implant Microsystem

Xin-Hong Qian, *Student Member, IEEE*, Yi-Chung Wu, *Student Member, IEEE*, Tzu-Yi Yang, Cheng-Hsiang Cheng, *Student Member, IEEE*, Hsing-Chien Chu, Wan-Hsueh Cheng, Ting-Yang Yen, Tzu-Han Lin, Yung-Jen Lin, Yu-Chi Lee, Jia-Heng Chang, Shih-Ting Lin, Shang-Hsuan Li, Tsung-Chen Wu, Chien-Chang Huang, Sung-Hao Wang, *Student Member, IEEE*, Chia-Fone Lee, Chia-Hsiang Yang, *Senior Member, IEEE*, Chung-Chih Hung, *Senior Member, IEEE*, Tai-Shih Chi, *Member, IEEE*, Chien-Hao Liu, *Member, IEEE*, Ming-Dou Ker, *Fellow, IEEE*, and Chung-Yu Wu, *Fellow, IEEE*

***Abstract*—*Objective:* To develop and verify a CMOS bone-guided cochlear implant (BGCI) microsystem with electrodes placed on the bone surface of the cochlea and the outside of round window for treating high-frequency hearing loss. *Methods:* The BGCI microsystem consists of an external unit and an implanted unit. The external system-on-chip is designed to process acoustic signals through an acquisition circuit and an acoustic DSP processor to generate stimulation patterns and commands that are transmitted to the implanted unit through a 13.56 MHz wireless power and bidirectional data telemetry. In the wireless power telemetry, a voltage doubler/tripler (2X/3X) active rectifier is used to enhance the power conversion efficiency and generate 2 and 3 V output voltages. In the wireless data telemetry, phase-locked loop based binary phase-shift keying and load-shift keying modulators/demodulators are adopted for the downlink and uplink data through high-*Q* coils, respectively. The implanted chip with four-channel high-voltage-tolerant stimulator generates biphasic stimulation currents up to 800 μA. *Results:* Electrical tests on the fabricated BGCI microsystem have been performed to verify the chip functions. The *in vivo* animal tests in guinea pigs have shown the evoked third wave of electrically evoked auditory brainstem response waveforms. It is verified that auditory nerves can be successfully stimulated and acoustic hearing can be partially preserved. *Conclusion* and *Significance:* Different from traditional cochlear implants, the proposed BGCI microsystem is less invasive, preserves partially acoustic hearing, and provides an effective alternative for treating high-frequency hearing loss.**

***Index Terms*—Active rectifier, bone-guided, cochlear implant, inductive link power supply, implantable medical devices.**

Manuscript received June 6, 2018; revised October 15, 2018 and December 19, 2018; accepted February 11, 2019. Date of publication February 25, 2019; date of current version October 18, 2019. This work was supported in part by the "Center for Neuromodulation Medical Electronics Systems" from the Featured Areas Research Center Program within the framework of the Higher Education Sprout Project by the Ministry of Education in Taiwan and in part by the Ministry of Science and Technology (MOST), Taiwan, under Project MOST-106-2221-E-009-160-MY2. *(Corresponding authors: Xin-Hong Qian; Chung-Yu Wu.)*

X.-H. Qian and C.-Y. Wu are with the Department of Electronics Engineering and the Institute of Electronics, National Chiao Tung University, Hsinchu 30010, Taiwan (e-mail: xinhongqian.ee99g@g2.nctu.edu.tw; peterwu@mail.nctu.edu.tw).

Y.-C. Wu is with the Graduate Institute of Electronics Engineering, National Taiwan University.

T.-Y. Yang, C.-H. Cheng, W.-H. Cheng, T.-Y. Yen, T.-H. Lin, Y.-J. Lin, Y.-C. Lee, S.-H. Wang, and M.-D. Ker are with the Department of Electronics Engineering and the Institute of Electronics, National Chiao Tung University.

H.-C. Chu, J.-H. Chang, S.-T. Lin, T.-C. Wu, C.-C. Hung, and T.-S. Chi are with the Department of Electrical and Computer Engineering, National Chiao Tung University.

S.-H. Li, C.-C. Huang, and C.-H. Liu are with the Mechanical Engineering Department, National Taiwan University.

C.-F. Lee is with the Department of Otorhinolaryngology, Buddhist Tzu Chi General Hospital and Tzu Chi University.

C.-H. Yang is with the Department of Electrical Engineering, National Taiwan University, and also with the Department of Electronics Engineering, National Chiao Tung University.

Digital Object Identifier 10.1109/TBME.2019.2901374

I. Introduction

COCHLEAR implants (CIs) or cochlear prostheses have successfully provided useful electrical hearing to more than 120,000 persons worldwide with serious sensorineural hearing loss [1], [2]. The CIs electrically stimulate the auditory nerves through an array of electrodes inserted into in the scala tympani of the cochlea. The electrode insertion causes complete loss of residual hearing and possibly the meningitis [1].

To eliminate the aforementioned risks, a bone-guided CI (BGCI) system-on-chip (SOC) microsystem with the electrodes deployed outside the cochlea is proposed and a preliminary version of this work has been reported [3]. In the BGCI microsystem, multiple electrodes are placed on the bone surface of the cochlea and one is on the outside of round window. The locations of these electrodes are near the base, which corresponds to the high frequency part of auditory nerve based on the tonotopic theory. Since the round window is not pierced and the structure of cochlea is left undamaged during the surgery, the acoustic hearing is partially preserved while providing electrical hearing. In order to evoke electrical hearing, the auditory nerves are stimulated by biphasic constant current pulses to maintain charge balance. Thus the tissue or electrode damages due to charge unbalance in monophasic stimulation can be avoided [4].

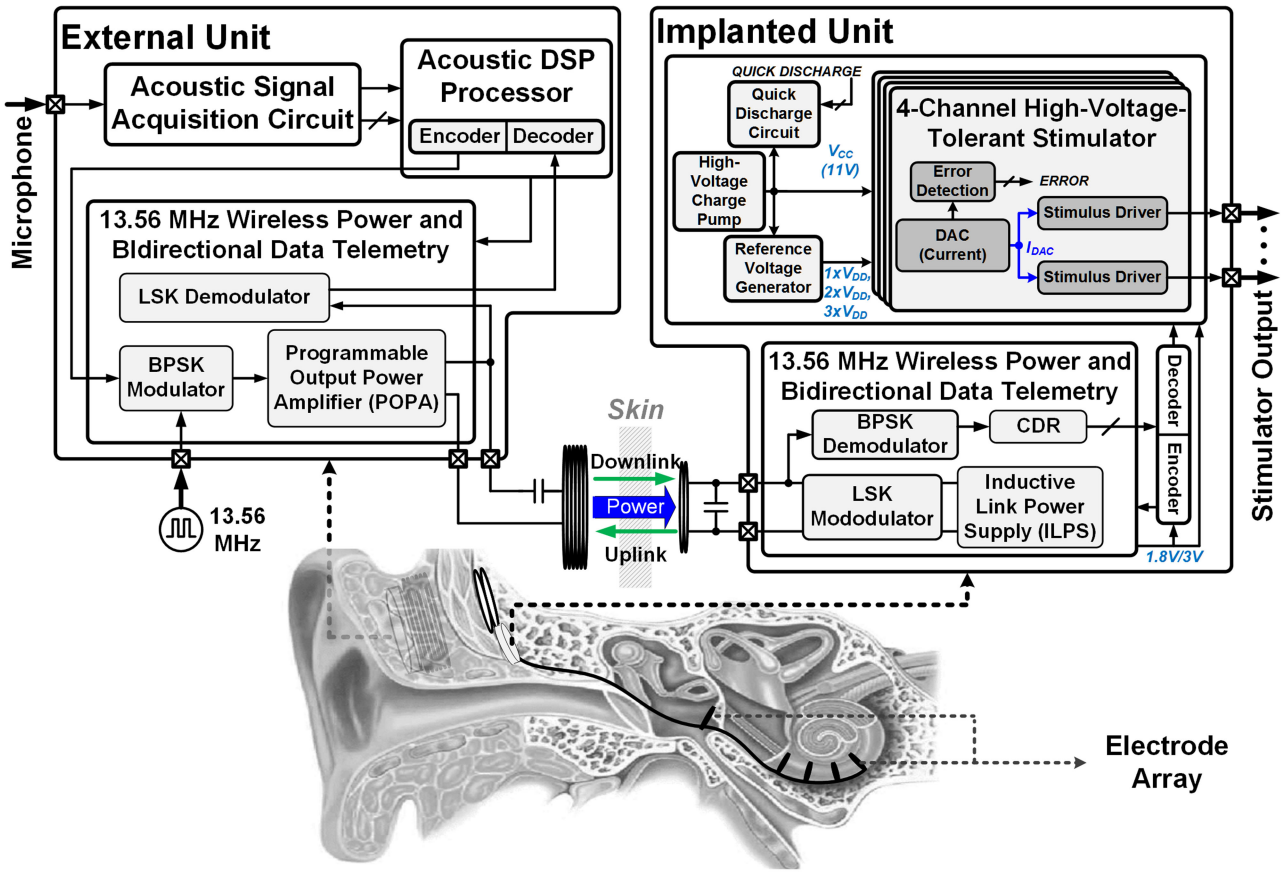

Fig. 1. Block diagram of the BGCI microsystem and the conceptual structure diagram of the BGCI microsystem placed in a human ear.

As compared with the conventional CIs, the BGCI has the following advantages: 1) It is minimally invasive and the acoustic hearing can be partially preserved. 2) It can be used to eliminate the symptoms for patients with high-frequency hearing loss while preserving the residual low-frequency hearing.

The architecture of the BGCI microsystem consists of the external unit and the implanted unit coupled through a pair of high-Q coils with ferrite cores [3]. In the external unit realized by a SOC, the acoustic signals are processed by a microphone and amplified and digitized by an acoustic signal acquisition circuit. Then the digitized signal is processed by an acoustic DSP to obtain the desired stimulation patterns in the frequency range of hearing loss. The frequency range is adjustable to support patients with high-frequency hearing loss. The patterns and the commands are further processed and transmitted with 13.56 MHz carrier signal through the primary coil into the secondary coil and the implanted unit. In the implanted unit, an inductive link power supply (ILPS) with forward data decoding and backward data encoding circuits is implemented to obtain wireless power and realize bidirectional data telemetry. A 4-channel high-voltage-tolerant stimulator is designed to generate biphasic constant current stimulus (CCS).

Under normal surgical operation, four electrodes can be put on the bone surface of human cochlea. According to psychoacoustic experiments in [5], four electrodes can achieve 80% speech discrimination. Once the frequency range of the high-frequency hearing loss in a patient is determined, it can be divided by 4 in the logarithmic axis to determine the central frequency of each electrode. As an example of high-frequency hearing loss between 4000 Hz and 8000 Hz, the central frequency of each channel can be 4367 Hz, 5199 Hz, 6182 Hz, and 7343 Hz with the frequency resolution of 1/4 octave. According to the results of EM simulation with the Finite Element Model (FEM) model of the cochlea [6], it is found that the electric field can be localized under the stimulating electrode on the cochlear bone. Thus acceptable frequency resolution and spatial specificity could be obtained for patients with high frequency hearing loss.

In this paper, in-vivo animal tests on guinea pigs on the CMOS BGCI microsystem are performed and the results are analyzed to verify its functions. It is shown from animal test results that the BGCI microsystem can successfully evoke the Wave eIII of EABR waveforms to recover the hearing capability of guinea pigs. Moreover, the acoustic hearing can be partially preserved when the BGCI microsystem is used.

This paper is organized as follows. Section II describes the system architecture and circuits of the BGCI microsystem for animal tests. Its experimental results of system electrical functions are also presented. Analyses and verifications of in-vivo animal tests on the BGCI microsystem are shown in Section III. Finally, the conclusion is drawn in Section IV.

II. System Architecture and Electrical Measurement Results

Fig. 1 shows the overall architecture of the BGCI microsystem and the conceptual structure diagram of the BGCI microsystem placed in human ear, where the external unit and the implanted unit are coupled through a pair of high-Q coils with ferrite cores. The external unit includes acoustic signal acquisition circuit and acoustic DSP whereas the implanted unit includes a 4-channel high-voltage-tolerant stimulator. An ILPS with bidirectional data transceiver is also designed in both units. The detailed circuits and functions of all components in the BGCI microsystem are described in the following [3].

A. Acoustic Signal Acquisition Circuit

The acoustic signal acquisition circuit in the BGCI microsystem is used to capture the acoustic signal from the microphone which plays a role as the connection between the nature voice and the electrical circuit. The acquisition circuit consists of a pre-amplifier and an analog-to-digital converter (ADC) [3]. The small acoustic signals from microphone are amplified and filtered by the pre-amplifier and then digitalized by the ADC for further digital processing.

The bandwidth is designed from 40 Hz to 200 kHz with the consideration of suppressing group delay. Its effective audio bandwidth is 40 Hz to 20 kHz. The gain of pre-amplifier can be adjusted in 0 dB, 3.5 dB, 6 dB, and 15.6 dB by the programmable feedback capacitor. The 40 Hz high-pass corner frequency can be implemented by the pseudo-resistors (PRs) connected in parallel with the programmable feedback capacitor. The pseudo-resistor can achieve 16 GΩ with the transistor size of channel width/length = 25.6 μm/0.8 μm. There is a flat region in the characteristics of impedance versus signal amplitude of the PR, where the impedance is almost constant like a normal resistor [7].

The amplified acoustic signals are directly sent to a successive-approximation-register (SAR) ADC with 10-bit resolution. The full-scale reference voltage $V_{\mathrm{ref,FS}}$ of SAR ADC is 0.9 V. The operational principle of the SAR ADC is the binary search to find the closest binary digital output to represent the analog input. The SAR ADC utilizes a monotonic capacitor switching procedure.

B. Acoustic DSP Processor

Fig. 2 shows the architecture of the acoustic DSP processor. The acoustic DSP processor consists of a reduced instruction set computer (RISC) core [8], hardware accelerators, a data en/decoder for wireless transmission, and peripherals. A spectral-change enhancement (SCE) algorithm [9], [10] is realized to improve speech intelligibility. According to the test results of [11], a significant improvement in speech reception threshold is achieved for the SCE algorithm. The RISC core is fully programmable and the hardware accelerators are added to improve the energy efficiency for realizing the SCE algorithm. The hardware accelerators include a 64-point real-valued fast Fourier transform (RFFT) unit and a data control unit (DCU).

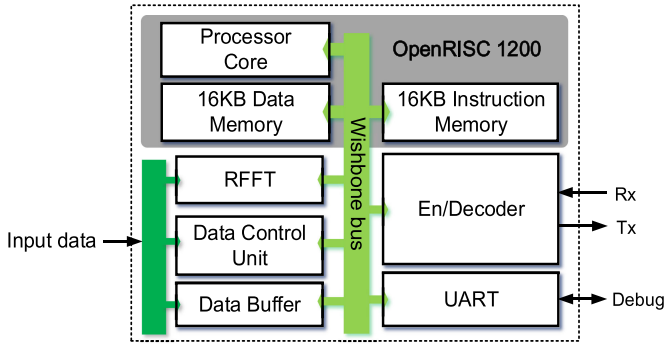

Fig. 2. Architecture of the acoustic DSP processor [3].

The RISC core contains a five-stage pipelined Harvard microarchitecture. It can connect with several modules through the wishbone bus. Each module is connected to a wrapper to establish a standard data exchange interface. The wrappers then communicate to each other by arbiters. In addition, a single design can feature multiple busses. Hardware accelerators are linked by the wishbone bus. IO interfaces, such as a joint test action group (JTAG), universal asynchronous receiver/transmitter (UART), and general-purpose input/output (GPIO), are also embedded. The JTAG is connected to a computer through a debugger module and is used to load the firmware onto the RISC core. The UART is mainly for debugging.

The acoustic signals are first sent to a RFFT unit to extract the spectrum. The magnitude of the frequency spectrum is reshaped based on the auditory excitation pattern [12] through a series of filtering to simulate band-pass filters in a normal auditory system. The outputs are then fed into a spectral change function to calculate the temporal difference. This function behaves as a temporal sharpening module on the spectrum. The difference of the spectra of interest is then amplified by a Difference-of-Gaussian (DoG) function, which mimics lateral inhibition of the auditory nerve to produce a spectral-contrast enhanced spectrum. The result is denoted as the enhancement function (ENF), which is the spectral and temporal enhanced spectrum. A temporal weighting function is then used to smooth the ENF by considering influences from preceding frames to finally generate the desired frequency spectrum for the stimulation channels. According to previous studies, the spectral contrast enhancement algorithms can improve speech intelligibility of hearing-impaired patients [9], [11], including CI user [13], under noisy conditions.

A RFFT unit is included to accelerate the computations for spectrum extraction. By leveraging the following properties, the proposed RFFT unit requires only half of the complexity of the complex-valued FFT one. Firstly, the redundant complex-valued operations can be removed before the real-valued signals encounter complex-valued twiddle factors. Secondly, multiplications with the same twiddle factors can be shared. Thirdly, half of the calculations related to the primary outputs can be omitted owing to the conjugate-symmetric feature. Folding and pipelining techniques have been proposed in [14], [15] to reduce area and power of realization of RFFT. A realized 64-point

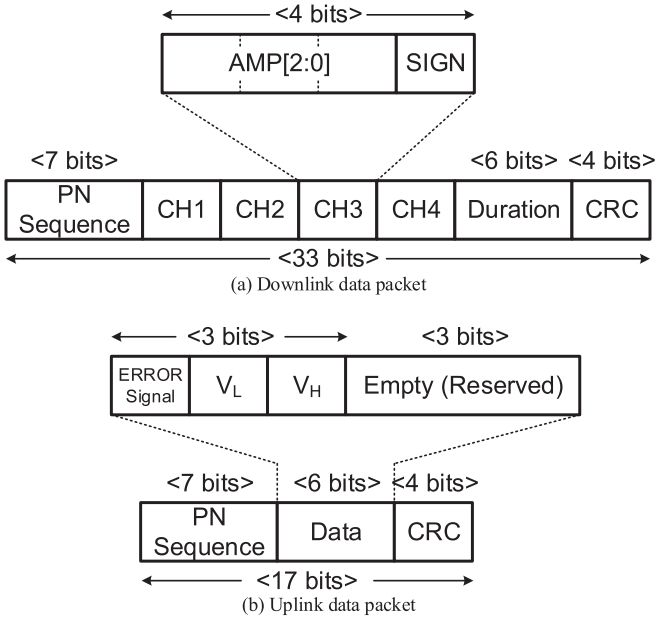

Fig. 3. The data codec and packet design in the BGCI with (a) downlink data packet and (b) uplink data packet.

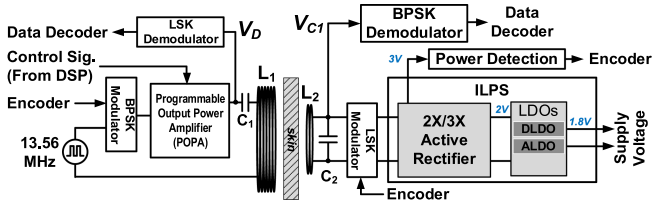

Fig. 4. Wireless power and bidirectional data telemetry circuit.

RFFT unit, which is included in this work, achieves 44% power savings as compared to the complex-valued FFT counterpart. For more details, the advantages of RFFT over complex-valued FFT have been discussed in the previous work [16].

A data control unit (DCU) is used to offload the data access for digitized inputs from the ADC, as shown in Fig. 2. The interrupt signal in DCU is triggered conditionally, rather than periodically, thereby reducing the time overhead caused by interrupt in this design.

The outputs of the SCE algorithm are stimulation patterns for 4 stimulation channels. In each channel, 3 bits (AMP[2:0]) are used to indicate the magnitude of stimulation currents and 1 bit (SIGN) is used for the polarity, as shown in Fig. 3(a). Additional 6 bits are included to identify the stimulation duration. There is a data encoder to transform it into a data packet for the wireless transmitter. As shown in Fig. 3(a), the downlink data packet contains a pseudo-random noise (PN) sequence for synchronization, a command (including magnitude, polarity, and duration) for the 4-channel high-voltage-tolerant stimulators, and an appended cyclic redundancy check (CRC) for error check. At the wireless receiver, there is also a decoder that receives and decodes the data packet in order to drive the high-voltage-tolerant stimulators. If a received data packet cannot pass the error check, it will be discarded and no electrical simulations are triggered.

In the BGCI microsystem, the continuous-interleaved-sampling (CIS) signal processing strategy is adopted, which has been implemented by many manufacturers in their latest devices [17], [18]. Using the CIS strategy to stimulate nerves with non-simultaneous and interleaved pulses in the BGCI microsystem is to avoid interaction between channels caused by the summation of electric fields from individual electrodes. The CIS strategy extracts multi-channel temporal envelopes and produces non-simultaneous interleaved stimuli across channels. Balanced biphasic pulse trains are delivered to electrodes with proper temporal offsets that eliminate any overlap across channels [19].

Vocoders are often used to simulate electrical hearing of CI patients. To simulate the hearing perception of the patient wearing the proposed BGCI microsystem, a vocoder was combined with the patient's personalized hearing model [20], which simulates the preserved acoustic hearing of the patient. To determine the proper settings for the BGCI microsystem, psycho-acoustic experiments were conducted on the hearing-model combined 4-channel vocoder to test the different frequency settings of the band-pass filters [5]. In the experiments, the cutoff frequency of the low-pass filter for envelope extraction was set to 400 Hz and the overall frequency range of the four band-pass filters was set to 4000–8000 Hz to provide high-frequency electrical hearing while preserving low-frequency acoustic hearing. Results of psycho-acoustic experiments reveal the four constant-Q band-pass filters distributing logarithmically with center frequencies of 4367 Hz, 5199 Hz, 6182 Hz, and 7343 Hz and the bandwidth of 1/4 octave provide benefits in enhancing Mandarin intelligibility scores of CI patients. A boost of 8%∼10% of intelligibility scores were observed in two simulated hearing-impaired patients and most of the improvement comes from consonants [5]. The consonants have high frequency energy above 4000 Hz, thus are presumably made clearer by the high frequency electric hearing provided by the 4-channel BGCI system. Details of the psycho-acoustic experiments can be accessed in [5]. These desired parameters of the filters are adopted by the acoustic DSP processor, which uses FFT magnitudes to encode the envelopes of the simulated vocoder and produces non-simultaneous interleaved stimuli to the 4 stimulation channels of BGCI microsystem.

C. Wireless Power and Bidirectional Data Telemetry Circuit

To avoid extra surgery for battery replacement, the power of implanted unit is supplied by the ILPS and the communication is realized by wireless bidirectional data transmission with 13.56 MHz as the carrier frequency. Fig. 4 shows the wireless power and bidirectional data telemetry circuit which consists of a programmable output power amplifier (POPA), a pair of high-Q coils, a 2X/3X active rectifier with LDOs, a BPSK forward data modulator/demodulator, and a LSK backward data modulator/demodulator. The high-Q coils with ferrite core is used to enhance the transfer efficiency of power and data telemetry in the proposed BGCI microsystem. The coil with ferrite core for the implant side can be wrapped and sealed with biocompatible material as in the conventional CIs. The BPSK demodulator

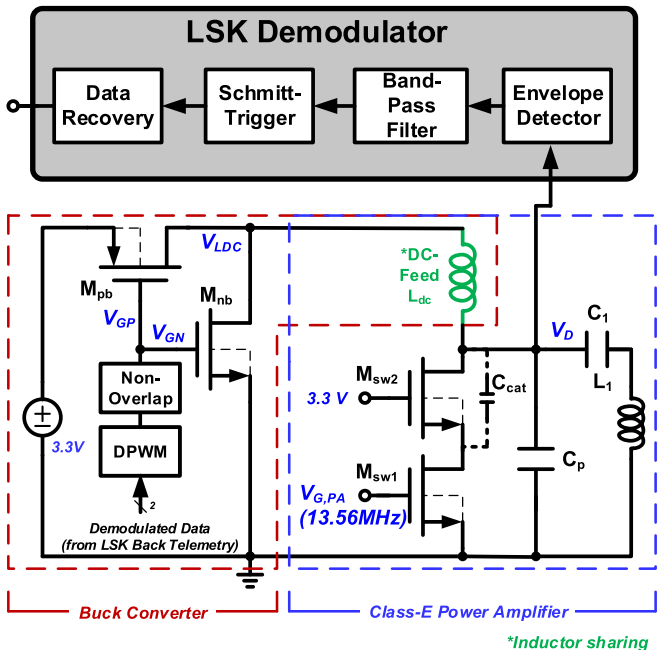

(a)

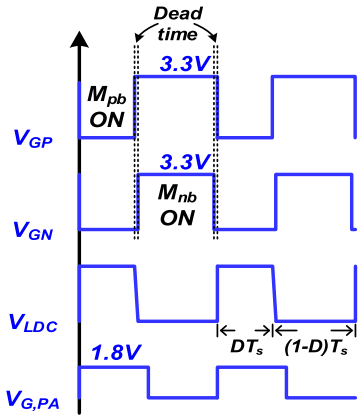

(b)

Fig. 5. (a) Architecture of 13.56-MHz CMOS class-E programmable output power amplifier (POPA) and LSK demodulator. (b) Control signals of 13.56-MHz CMOS class-E programmable output power amplifier (POPA).

is adopted to demodulate the data from the external unit without much degrading the high power transfer efficiency through the high-Q of near-field coil. However, the high-Q coils cause the decrease in data channel capacity. When a downlink BPSK data transition occurs, the secondary coil requires a few cycles to invert its phase. Thus the conventional edge-detector BPSK demodulator [21] cannot work properly because of the longer data transition time. Thus the PLL-based BPSK demodulator is adopted [22]. The LSK demodulator consists of an envelope detector, a band-pass filter, a Schmitt-trigger, and a data recovery unit to demodulate the data from the output node of the POPA as shown in Fig. 5(a).

Fig. 5(a) also shows the programmable output power amplifier (POPA), which consists of a digital pulse-width modulator (DPWM), a buck converter, and a class-E power amplifier with

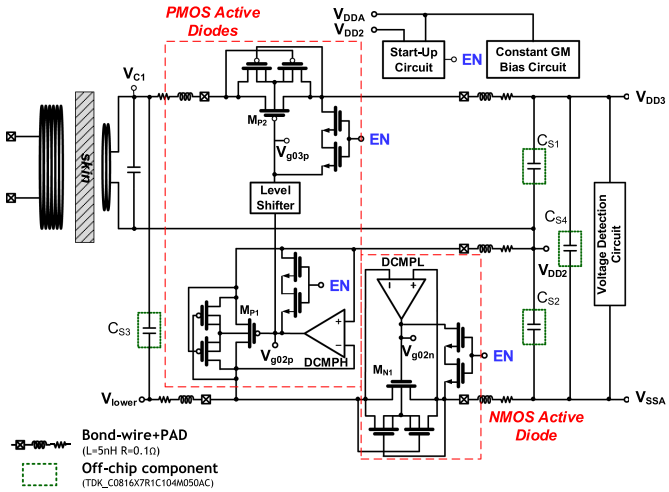

Fig. 6. The circuit structure of 2X/3X active rectifier.

a finite DC-feed inductor. The DPWM is used to produce a control signal with fixed frequency and variable duty cycle D for buck converter as shown in Fig. 5(b). The DPWM is controlled by the demodulated data from LSK back telemetry, which is a set of pulse signals with 2-bit voltage magnitude information of 3X active rectifier in the implanted unit. The control signal with variable duty cycles in the buck converter generates different supply voltages for the class-E power amplifier and thus different output powers. When the output voltage of 3X active rectifier is lower (higher) than the preset threshold 3 V (3.2 V), the duty cycle of buck converter is increased (decreased) and the energy stored in the inductor increases (decreases) accordingly. Therefore, the POPA can deliver more (less) power by increasing (decreasing) the duty cycle of control signal in the buck converter and thus generate higher (lower) output power.

The cascode-transistor configuration in the class-E power amplifier (PA) can have a higher reliability without voltage overstress as shown in Fig. 5(a). The gate of cascode transistor M_{SW2} is driven by a 3.3 V bias so that the drain voltage V_D of M_{SW2} can tolerate 6.6 V voltage without device stress. In addition, using a finite DC-feed inductance instead of an RF-choke in the class-E PA can generate a larger output power under the same supply voltage [23], [24]. In this work, the buck converter is designed to share the finite DC-feed inductor of power amplifier without using an extra inductor.

The circuit structure of the 2X/3X active rectifier of ILPS is shown in Fig. 6, which consists of a start-up circuit, a NMOS active diode, two PMOS active diodes, two delay-compensated comparators (DCMPH and DCMPL) with delay compensation control, a level shifter, and off-chip filtering capacitors.

In Fig. 6, the comparator DCMPH (DCMPL) controls the power transistor M_{P1} (M_{N1}) by comparing the voltage V_{lower} and V_{DD2} (V_{lower} and V_{SSA}). The two PMOS active diodes of 2X/3X active rectifier only need a single comparator DCMPH to control both power transistors M_{P1} and M_{P2}. However, since the PMOS power transistor M_{P2} is operated in a higher voltage level than M_{P1}, a level shifter is needed to convert the control signal from low voltage level to high voltage level for M_{P2}. In

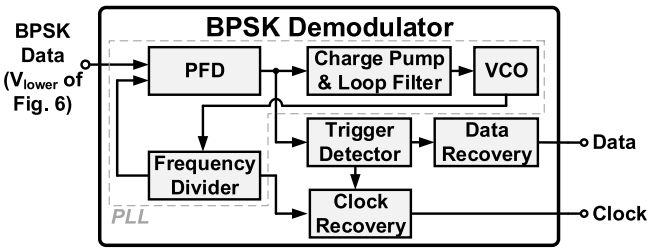

Fig. 7. Block diagram of PLL-based BPSK demodulator.

Fig. 6, the voltage level of the output voltage V_{g02p} of DCMPH is from 0 V to V_{DD2} (2 V). Since the I/O device can handle 3.3 V in 0.18 μm CMOS technology, a simple level shifter can be designed by using I/O devices to convert the voltage level from V_{DD2} to V_{DD3} (3 V) without device over-stress issue. It converts the voltage level and enhance the driving ability to drive the large input capacitance of power transistor M_{P2}.

In the design of 2X/3X active rectifier in Fig. 6, both over voltage protection (OVP) and under voltage protection (UVP) realized by the voltage detection circuit are used to make sure that the output voltage V_{DD3} neither exceed 3.3 V to avoid the device over-stress issue nor decrease below 3 V to cause the high-voltage charge pump unable to reach the specified output pump voltage.

The data packet of LSK back telemetry contains both the V_L and V_H as shown in Fig. 3(b). When the LSK back telemetry is enabled, the external unit gets the backward data packet. After demodulation and decoding, the voltage amplitude information of 3X active rectifier of the implanted unit is sent to the POPA. If V_{DD3} is higher (lower) than 3.2 V (3 V), the POPA can reduce (increase) the transmitted energy to the primary coil.

The PLL-based BPSK demodulator [22] can demodulate BPSK signal through the high-Q coil L_2 and fully integrated with the ILPS as shown in Fig. 4. The carrier frequency of coil L_2 changes slowly when the phase of carrier frequency of coil L_1 changes 180 degrees. Since the transition time of high-Q coil L_2 is longer, a PLL is used to detect the frequency change during data transition. The block diagram of BPSK demodulator is shown in Fig. 7 [22] which consists of a PLL, a trigger detector circuit, and data and clock recovery circuits. The PLL consists of phase frequency detector (PFD), charge pump (CP), loop filter, voltage control oscillator (VCO), and frequency divider.

The PFD detects the phase and frequency difference between input signal and feedback signal and generates short duration pulses at the output with minimum dead zone when PLL is locked. During the data transition where the frequency of PFD input is changed, it generates output control signals for CP to alter the VCO and change the output frequency to lock the new frequency. At the same time, the trigger detector uses a pulse collector circuit to collect these longer duration pulses from the PFD. The pulse collector circuit is used to combine the multiple longer duration pulses to form a single wider pulse-width signal when the pulse width of longer duration pulses exceeds a preset threshold. After the wider pulse-width signal has been detected, a trigger signal is produced to invert the current demodulated data (e.g., high level to low level). In the clock recovery circuit, a divided-by-64 frequency divider is used to divide the carrier frequency of 13.56 MHz to generate 211 kHz clock signal. However, during the data transition, the carrier frequency changes. So, after a long time, the clock edge is not synchronized with the demodulated data. Therefore, the trigger signal is also used to reset the divider after the trigger signal is raised. And then, the divider is reset and the clock is synchronized with the output demodulated data. Finally, the data and clock can be decoded by the decoder. The data is sent to the stimulators to generate the corresponding stimulation current.

D. High-Voltage-Tolerant Stimulator

The high-voltage-tolerant stimulator consists of 4 stimulus channels, a high-voltage charge pump, a reference voltage generator, a quick discharge circuit, 4 stimulus channels each containing a pair of stimulus drivers in the H-bridge topology, a current-mode DAC, and an error detector [25] as shown in Fig. 1. The maximum output voltage (V_{CC}) of high-voltage charge pump is 11 V which is the supply voltage of stimulus channels. The V_{CC} (11 V) is divided into 3 levels ($1xV_{DD}$, $2xV_{DD}$, and $3xV_{DD}$) through a reference voltage generator to provide the required reference voltages for the self-adaption bias circuit and level shifter circuits of the stimulus drivers. The quick discharge circuit can discharge V_{CC} when the QUICK DISCHARGE signal is received. The stimulus driver delivers biphasic stimulus current through two electrodes and provides stimulation on the acoustic nerves between the electrodes. The error detector in the stimulus driver detects the load impedance to see whether it is in the normal range for maximum voltage (11 V) and maximum current (0.8 mA) operation. The normal range of the load impedance is defined as the electrode-tissue double-layer capacitance [26] larger than 10 nF and the tissue resistance smaller than 14 kΩ. If the impedance of electrode-tissue interface exceeds the normal range, the error detector raises an alert signal to indicate the possible abnormal operation. This ERROR signal is also included in the data packet of LSK back telemetry as can be seen in Fig. 3(b).

To adapt to a wide range of load impedances of the electrode-cochlea interface, stacked transistors and a self-adaption bias circuit are used in the stimulus driver which can detect the output node voltage and adjust the suitable bias for stacked transistors to prevent overstressed problems [25].

In each stimulation, one electrode on the bone surface is selected and the electrode on the round window is also selected. The bipolar and biphasic constant current stimulation (CCS) is realized by sending a constant current to the selected electrode on the bone surface with the electrode on the round window grounded first to inject charges to the auditory nerves in the scala tympani of the cochlea through electric field for stimulation. Then the same constant current is sent to the electrode on the round window with the electrode on the bone surface grounded to balance the injected charges and avoid any accumulated charges in tissues or nerves for safety consideration. Such a biphasic CCS is performed successively for the 4 electrodes on the bone surface.

In the BGCI microsystem, the CIS signal processing strategy is adopted. For the four-electrode BGCI system, only one stimulation is performed in each time. Thus only one current source is used to save power. The current source is shared alternatively by the four electrodes.

E. Results of Electrical Measurement

The BGCI microsystem was designed and fabricated in 0.18-μm CMOS Technology. The SOC chip of the external (implanted) unit occupies 12.26 mm^2 (7.26 mm^2) including the ESD pads. Each circuit was tested separately and the function of the whole system was verified in both electrical tests and animal test.

The measurement results of the fabricated acoustic signal acquisition circuit are summarized as below. The measured 4 levels of gains of the pre-amplifier with different setting are 0 dB, 3.5 dB, 6 dB, and 15.6 dB with the bandwidth of 40 Hz to 20 kHz. The design of these pre-amplifier gains is based on the requirement of the whole BGCI microsystem. The 16-dB programmable gains of the pre-amplifier and the 62-dB dynamic range of the 10-bit ADC are combined to cover the typical 80-dB input dynamic range. They were designed together with the considerations of the weighting factors in the acoustic DSP processor, and the output currents of the stimulator. The system uses the four tunable gains of the pre-amplifier, weighting factors in the acoustic DSP processor, and the output currents of the stimulator to make the output stimulation remaining within the comfortable listening levels of the patients.

Since the output current from the pre-amplifier is used to drive the following capacitor array of the SAR ADC, the pre-amplifier consumes about 501 μW. The measured differential nonlinearity (DNL) and integral nonlinearity (INL) of the SAR ADC are both less than 0.24 LSB. The signal-to-noise-and-distortion-ratio (SNDR) is 60.09 dB with 1 kHz sinusoid input. The power dissipation is 20.94 μW. The figure of merit (FOM) [27] is 528.4 fJ per conversion-step in the audio band where the FOM is the power dissipation divided by the term of $fs \cdot 2^{ENOB}$.

The acoustic DSP dissipates 7.78 mW at 25 MHz from a 1 V supply. The overall latency of the signal processing of the SCE algorithm is 1.33 ms. The latency of the signal processing of the SCE algorithm for a system with more channels would be nearly the same since only the computations for channel combination, which accumulates the energy for the required channel bins, in the last stage need to be changed.

The measured maximum power conversion efficiency (PCE) of the POPA, which consists of buck converter and class-E power amplifier, is 62.5%. The measured PCE of the ILPS, composed of active rectifier and LDOs, is 59% under 25 mW output power level with the coil separation of 10 mm. If the coil separation is decreased (increased), the PCE will be increased (decreased). Fig. 8 shows the measured PCE of 2X/3X active rectifier versus different output power levels. In the light load condition, the switching loss dominates and the PCE is decreased. The fabricated 2X/3X active rectifier can provide 3 V and 2 V output voltages and the maximum power capability is up to 55 mW.

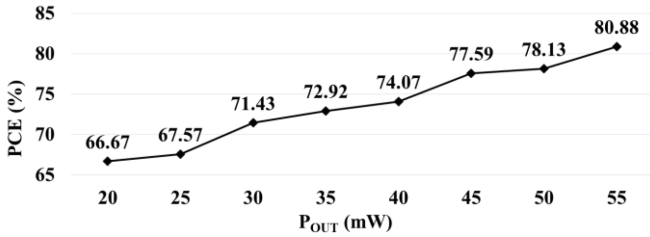

Fig. 8. The measured power conversion efficiency (PCE) of 2X/3X active rectifier versus output power.

TABLE I
THE PERFORMANCE SUMMARY OF THE PROPOSED BGCI MICROSYSTEM

Parameter		Performance
Placement of Electrode Arrays		Bone surface of the cochlea, round window
Preservation of Acoustic Hearing with Cochlear Implantation		Yes
Core Voltage Supply (V)		1.8/3
Chip Areas		External: 12.26 mm^2 Implanted: 7.26 mm^2
Near-Field Coils with Ferrite Core	External Coil	Diameter: 3 cm Thickness: 1.91 mm
	Implanted Coil	Diameter: 2.2 cm Thickness: 1.91 mm
Acoustic Signal Acquisition Circuit	Audio Frequency Range (Hz)	40–20k
	Gain (dB)	0/3.5/6/15.6
	SNDR (dB)	60.09
	ENOB	9.69@48kS/s
	INL/DNL (LSB)	0.24/0.24
	FOM (fJ/conversion-step)	528.4
Acoustic DSP Processor	Power Dissipation (mW)	7.78 (25 MHz, 1 V)
	Overall Latency (ms)	1.33
Wireless Power and Data Telemetry	Carrier Frequency (MHz)	13.56
	PCE of ILPS	59%@25mW
	Forward Command Link/ Backward Data Link	BPSK/ LSK
	Max. Data Rate (kbps)	339 (Downlink), 105 (Uplink)
High-Voltage-Tolerant Stimulator	Number of Electrodes	4
	Supply from High-Voltage Charge Pump (V)	11
	Pulse Width (μs/phase)	24-146@212kbps
	Max. Stimulation Current for Rats (mA)	0.8
	Max. Stimulation Rate (pps/ch)	750

The overall PCE from buck converter to the high-voltage charge pump in the stimulator stage is about 15% where the PCEs for the components in the power system are: buck converter 87%, class-E power amplifier 72%, coils 76%, ILPS 59%, and high-voltage charge pump 53%.

In the bidirectional data telemetry, the fabricated BPSK demodulator with 332 μW power consumption or 0.98 nJ per bit has the measured maximum data rate of 339 kbps. The fabricated LSK modulator has the measured maximum data rate of 105 kbps. The fabricated stimulator can deliver 200 μA to 800 μA (100 μA per step) stimulus current to the electrodes for animal test. The power consumption of the proposed external (implanted) SOC is 131.35 mW (41.11 mW). The performance summary of the proposed BGCI microsystem for animal tests is shown in Table I.

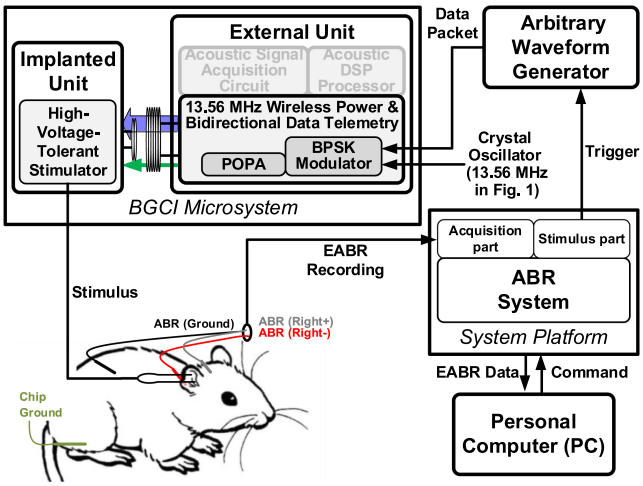

Fig. 9. The experimental setup of animal in-vivo tests.

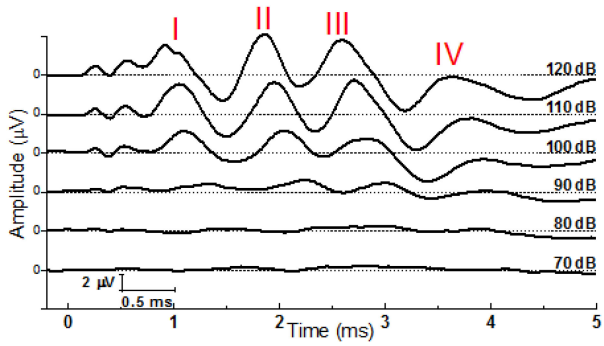

Fig. 10. Measurement results of acoustic hearing tests with click sound, which has duration of 50 μs, for the cochlea of guinea pigs. The measured peaks of Waves I, II, III, and IV of the evoked ABR become obvious when sound pressure level (SPL) of click sound is increased from 70 dB to 120 dB.

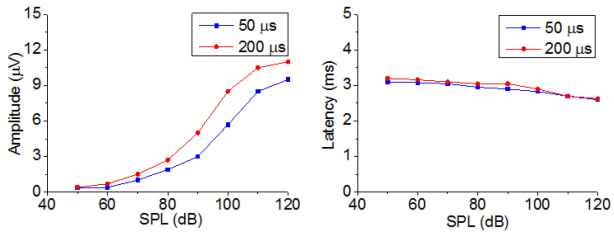

Fig. 11. The measured ABR characteristics under the click sound tests. Left: The measured amplitude of the evoked Wave III on ABR versus sound pressure level (SPL). Right: The measured latency of the evoked Wave III on ABR versus SPL.

III. Results of Animal Tests

Besides the electrical test, the proposed BGCI microsystem was tested in-vivo on guinea pigs to verify its functionality. Fig. 9 shows the experimental setup of animal in-vivo test where the BGCI microsystem, an arbitrary waveform generator, a commercial auditory brainstem response (ABR) system, and a personal computer (PC) are used. As shown in Fig. 9, the PC delivers continuous real-time commands to the stimulus part of ABR system, which transmits a trigger signal to the arbitrary waveform generator. Then the arbitrary waveform generator sends a set of packet data to the BPSK modulator in the external part of the BGCI microsystem. The BPSK data modulate the 13.56 MHz power signal generated by a crystal oscillator and both power and data are transmitted through the primary coil to the secondary coil. The implanted unit of BGCI microsystem receives wireless power and packet data from the secondary coil to drive the high-voltage-tolerant stimulator and enable the biphasic current stimulation. After electrical stimulation of the cochlear nerve, the electrically evoked ABR (EABR) potentials is recorded by the acquisition part of ABR system. The final recorded data are obtained by calculating the average values from 200 sets of valid measurement data.

Guinea pigs were anesthetized by initial intraperitoneal injection of sodium pentobarbital (35 mg/kg body weight). The maintenance dose of 10 milligram per kilogram (10 mg/kg) body weight was given throughout an experiment whenever the animal showed signs of increasing arousal, which was assessed every 30 minutes by a paw withdrawal reflex. Acoustic hearing tests using click sound were performed first. As shown in Fig. 10, the evoked ABR by acoustic hearing tests shows the measured peaks of Wave I. II. III. and IV versus sound pressure level (SPL) of click sound. It can be seen that the peaks become obvious as the SPL is larger than 70 dB. This ensures that the experimental setup was established correctly and the initial physiological condition of the cochlea can be obtained. The measured amplitude and latency of the evoked Wave III on ABR versus SPL are recorded and shown in Fig. 11 where the click-sound durations of 50 μs and 200 μs were used. Usually, the evoked ABR can be observed when the SPL is larger than the threshold of 50–60 dB.

Then a dermal incision was made from the lower right jaw to the shoulder to expose the right submandibular gland and the right submandibular gland was partially removed. The muscles attached to the bulla and the styloid bone were carefully dissected. Next, the bulla was opened to allow the access to the cochlear bone. Since the size of cochlear bone in guinea pigs is small, one electrode on the middle part of cochlear bone and the other electrode on the outside of round window were used in the animal in-vivo study to verify the functions of the designed BGCI microsystem. Two types of electrodes with electrode plate diameter D and length L were used as Type A (D = 300 μm and L = 2000 μm, 50 μm in thickness, gold) and Type B (D = 400 μm and L = 1000 μm, 50 μm in thickness, gold). The anatomy of the ear of guinea pig with the placement of electrode pairs is shown in Fig. 12 where one electrode was placed on the surface of the cochlear bone and the other on the outside of round window.

Both ABRs and EABRs were measured by the acquisition part of ABR system. The recording parameters are as follows: stimulation rate of 25 stimulus per second, 100 Hz to 3 kHz band-pass filters, amplification gain of 100K, and analysis time window of 12 ms. The care and use of the animals in this study were accordance with National Taiwan University College of Medicine

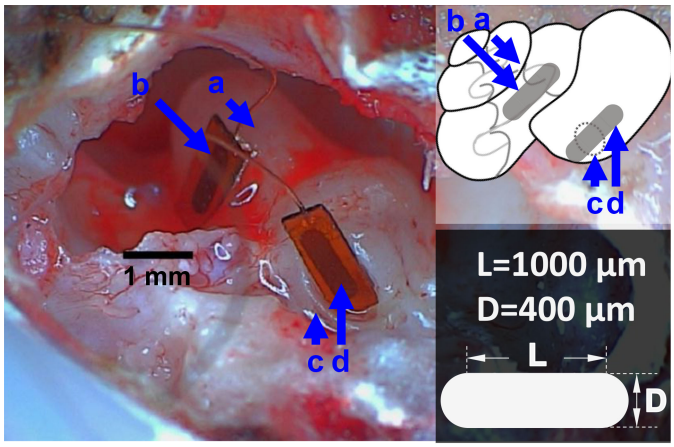

Fig. 12. The anatomy of the ear of guinea pig and the placement of Type B electrode pairs where **a**: the surface of cochlear bone; **b**: the electrode on the surface of cochlear bone; **c**: round window; **d**: the electrode on the round window. The scale bar is 1 mm.

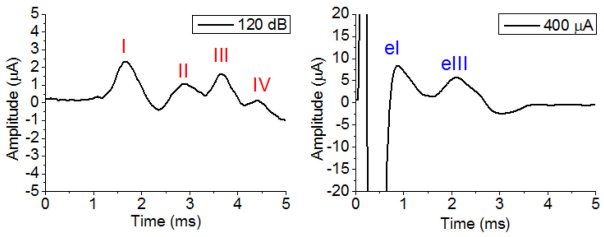

Fig. 13. Measurement results of ABR and EABR from in-vivo animal tests on guinea pigs. Left: The measured waveform of the evoked ABR under the acoustic test with 120 dB of SPL and total duration of 200 μs. Right: The measured waveform of the evoked EABR under the electrical stimulation of 400 μA biphasic current and pulse width of 100 μs/phase through Type A electrodes.

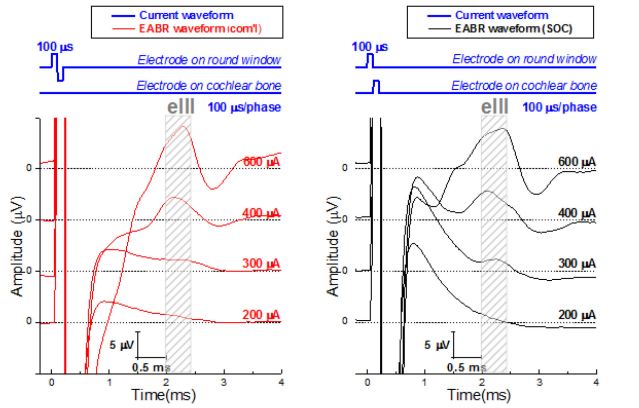

Fig. 14. Measurement results of in-vivo animal tests on guinea pigs with Type A electrodes. The measured Wave eIII of EABR waveforms under different stimulation currents generated by a commercial stimulator (red lines) and the proposed BGCI microsystem (black lines).

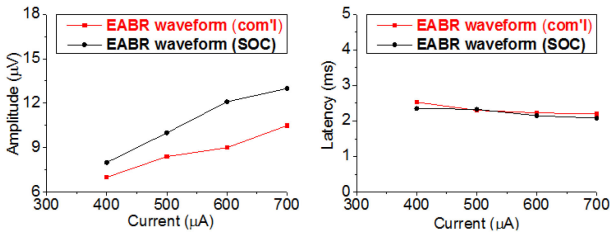

Fig. 15. The measured amplitude (left) and latency (right) of evoked Wave eIII on EABR versus stimulation currents generated by a commercial stimulator (red lines) and the proposed BGCI microsystem (black lines). The electrodes are of Type A.

and College of Public Health Institutional Animal Care and Use Committee (IACUC) with approval number 20150008.

Fig. 13 shows the measured ABR and EABR waveforms. The measured ABR under the SPL of 120 dB has an amplitude of only several microvolts. But the measured EABR has a shorter latency and a larger amplitude of several tens microvolts. The latency of Wave eIII in the recorded EABR is at approximately 2 ms as reported in [28], [29].

As shown in the Fig. 14, EABRs were recorded under biphasic current stimulations with a pulse width of 100 μs/phase and different current levels from 200 μA to 600 μA generated by a commercial stimulator (red lines) and the BGCI microsystem (black lines). In using commercial stimulator, the electrode on the bone was grounded and the electrode on the round window was stimulated by positive/negative biphasic currents. In using BGCI microsystem, positive current is applied to the electrode on the round window first and then the electrode on the bone after 5 μs. It is seen from Fig. 14 that the evoked Wave eIII of EABR waveforms can be recorded when the stimulation currents higher than 300 μA from the BGCI microsystem or the commercial stimulator. Moreover, the recorded EABR waveforms are similar in both cases under the same level of stimulation current.

In the BGCI microsystem, electrodes were placed on the surface of the cochlear bone instead of being inserted through the round window. Due to the high impedances of cochlear bones, the threshold stimulation current of 300 μA is needed to evoke Wave eIII, which is higher than that of conventional CIs. The stimulation current of 300 μA of BGCI microsystem did not damages the cochlea. The measured eIII wave responses are resulted from the auditory nerves because the latencies and morphology of nerve responses are similar to the previous study [29], [30]. In addition, nerve responses could not be detected by transecting auditory nerve in the end of experiments.

Since the electrodes of BGCI are put on bone surface of the cochlea, the bone of human cochlea will be thinned to reduce the thickness before electrode implant. But the electrodes are still not close to the auditory nerve. Thus, it requires a higher threshold current for activating auditory nerve and the stimulation power efficacy is not as high as the conventional CI. The higher threshold current has been verified in animal tests as shown in Fig. 15.

The frequency resolution in stimulation cannot be verified in current animal tests without opening the skull and using the microelectrode array to record the brainstem activities. It will

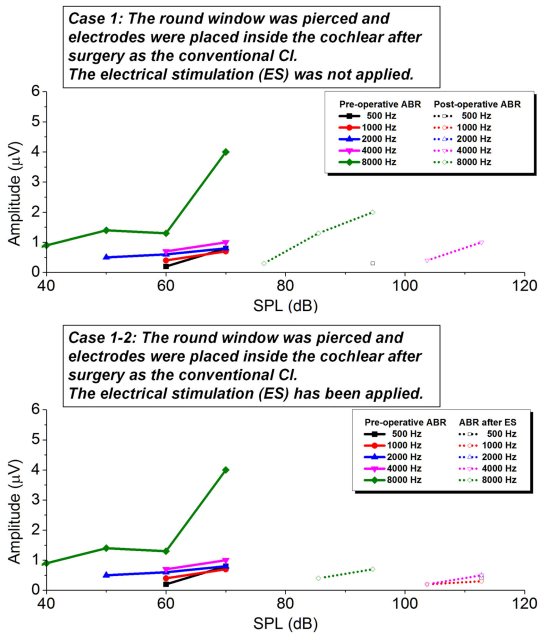

Fig. 16. The measured amplitudes of pre-operative ABR (solid line) and post-operative ABR (dash line) versus SPL on guinea pigs by tone-burst sound tests where the round window was pierced and electrodes were placed inside the cochlea after surgery as in the conventional CI. The electrical stimulation was not applied (upper) and after the electrical stimulation has been applied (lower).

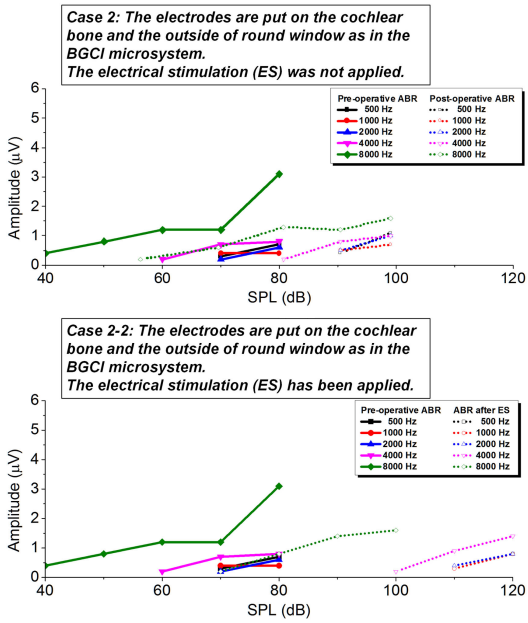

Fig. 17. The measured amplitudes of pre-operative ABR (solid line) and post-operative ABR (dash line) versus SPL on guinea pigs by tone-burst sound tests where electrodes are put on the cochlear bone and the outside of round window as in the BGCI microsystem. The electrical stimulation was not applied (upper) and after the electrical stimulation has been applied (lower) with Type A electrodes.

be performed to verify the frequency resolution in the future. The spatial specificity in stimulation cannot be verified in animal tests. According to the results of EM simulation with the Finite Element Model (FEM) model of the cochlea [6], it is found that the electric field can be localized under the stimulating electrode on the cochlear bone. Thus acceptable frequency resolution and spatial specificity could be obtained for patients with high frequency hearing loss.

The measured amplitude and latency of evoked Wave eIII on EABR versus stimulation currents are shown in Fig. 15 where the stimulation currents were generated by a commercial stimulator (red lines) and the proposed BGCI microsystem (black lines). The electrodes are of Type A. As shown in the left of Fig. 15, when the stimulation current is increased, the amplitude of Wave eIII is also increased. But the latency of Wave eIII is insensitive to stimulation currents as can be seen in the right of Fig. 15.

To measure the partial preservation of acoustic hearing after the implant of BGCI microsystem on guinea pigs with electrodes put on the cochlear bone and the outside of round window, the ABR amplitudes versus SPL before implant (pre-operative ABR) and after implant (post-operative ABR) by tone-burst sound tests were measured. The same tests were also performed on guinea pigs where the round window was pierced and electrodes were placed inside the cochlea after surgery as in the conventional CI. Fig. 16 shows the measured amplitudes versus SPL of pre-operative ABR and post-operative ABR in the case of conventional CI (Cases 1 and 1–2). In the upper part of Fig. 16, since the electrode pairs were inserted into the cochlea through the round window, the attenuation of residual acoustic hearing is very serious after surgery. After the electrical stimulation, the residual hearing is almost disappeared as shown in lower part of Fig. 16.

Fig. 17 shows the measured amplitudes versus SPL of pre-operative ABR and post-operative ABR in the case of BGCI microsystem (Cases 2 and 2–2). In the upper part of Fig. 17 where the electrodes were not stimulated, the threshold difference in SPL between pre-operative ABR and post-operative ABR is due to the opening the bulla cavity of guinea pig [31]. In lower part of Fig. 17 where electrical stimulation has been applied through electrodes, the acoustic hearing is still partially preserved since the round window is not pierced during the surgery and the placement of electrodes are on the outside of round window. It can be seen that the difference between pre-operative ABR and post-operative ABR was increased after the stimulating current had been applied. This could be owing to the long stimulating and the anesthesia status of nerves in guinea pigs. In Fig. 17, the ABR cannot be detected below about 60 dB SPL. The acoustic threshold of 60 dB SPL is because the guinea pigs in anesthesia status. Thus the animal tests on the guinea pigs cannot measure the responses to quiet sounds.

In-vivo animal tests on guinea pigs were also performed where the electrical stimulation and acoustic hearing test with click sound were applied simultaneously and both EABR and ABR were recorded. In Fig. 18, the evoked Wave eIII of EABR were recorded under the electrical stimulation of 500 μA biphasic current and pulse width of 100 μs/phase through Type B electrodes. The evoked Wave IV of ABR were also recorded

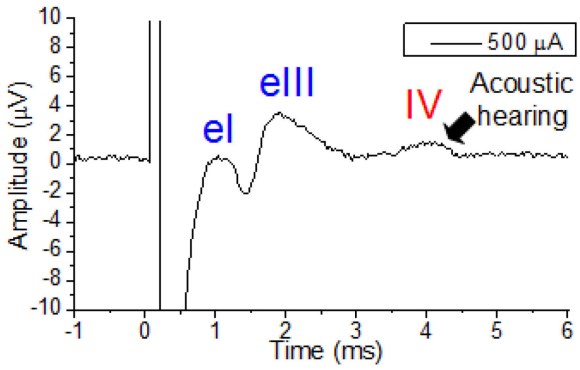

Fig. 18. Measurement results of ABR and EABR from in-vivo animal tests on guinea pigs. Both EABR and ABR were recorded when the electrical stimula-tion and acoustic hearing test with click sound were applied simultaneously. It provides an evidence to show that auditory nerves can be successfully stim-ulated and acoustic hearing can be partially preserved.

when the acoustic hearing test with click sound was applied. As the result, the acoustic hearing is still preserved partially (red arrow) while the biphasic current stimulation enables electrical hearing.

From the ABR measurement results of Fig. 16 Fig. 18, it is verified with experimental evidence that auditory nerves can be successfully stimulated and acoustic hearing can be partially preserved when the BGCI microsystem is used.

IV. Conclusion

The CMOS bone-guided cochlear implant (BGCI) SOC microsystem has been designed and in-vivo animal tests on guinea pigs have been performed for function verification. In the BGCI microsystem, electrodes are placed on the bone surface of the cochlea and the outside of the round window so that the acoustic hearing can be partially preserved after implant. It can be used to eliminate the symptoms for patients with high-frequency hearing loss while preserving the residual low-frequency hearing.

In the external SOC of BGCI microsystem, the acoustic signal is processed by the acquisition circuit followed by the acoustic DSP processor which is realized with low power real-value FFT and spectral-change enhancement algorithm. Then the stimulation patterns and commands are generated and transmitted to the implanted chip through the 13.56 MHz wireless power and bidirectional data telemetry using a pair of high-Q coils. A novel 2X/3X active rectifier with 2 V and 3 V output voltages can deliver power up to 55 mW. The BPSK downlink and the LSK uplink data telemetry are designed with the power telemetry. The PLL-Based BPSK demodulator can achieve the data rate up to 339 kbps. The 4-channel high-voltage-tolerant stimulator with biphasic stimulation currents up to 800 μA is designed in the implanted chip. Electrical tests have been successfully performed to verify the functions.

Animal in-vivo tests on guinea pigs have been performed. It is shown that the BGCI microsystem can evoke the auditory nerve in cochlea and generate the Wave eIII in the EABR waveforms while preserving partially the acoustic hearing. Future research will be conducted on the proposed BGCI microsystem for human clinical trial.

Acknowledgment

The authors would like to thank National Chip Implementation Center (CIC) for Chip design environment support.

References

[1] F.-G. Zeng *et al.*, "Cochlear implants: System design, integration, and evaluation," *IEEE Rev. Biomed. Eng.*, vol. 1, pp. 115–142, 2008.
[2] F.-G. Zeng *et al.*, "Development and evaluation of the Nurotron 26-electrode cochlear implant system," *Hear. Res.*, vol. 322, pp. 188–199, Apr. 2015.
[3] X.-H. Qian *et al.*, "A bone-guided cochlear implant CMOS microsystem preserving acoustic hearing," in *Proc. Symp. VLSI Circuits. Dig. Tech. Papers*, 2017, pp. C46–C47.
[4] D. R. Merrill, "The electrochemistry of charge injection at the electrode/tissue interface," in *Implantable Neural Prostheses 2: Techniques and Engineering Approaches*. New York, NY, USA: Springer-Verlag, 2010, pp. 85–139.
[5] T.-C. Wu *et al.*, "Simulations of high-frequency vocoder on Mandarin speech recognition for acoustic hearing preserved cochlear implant," in *Proc. Annu. Conf. Int. Speech Commun. Assoc.*, 2017, pp. 196–200.
[6] C.-F. Lee *et al.*, "Registration of micro-computed tomography and histological images of the guinea pig cochlea to construct an ear model using an iterative closest point algorithm," *Ann. Biomed. Eng.*, vol. 38, no. 5, pp. 1719–1727, May 2010.
[7] H. Kassiri *et al.*, "Low-distortion super-GOhm subthreshold-MOS resistors for CMOS neural amplifiers," in *Proc. IEEE Biomed. Circuits Syst. Conf.*, Oct. 2013, pp. 270–273.
[8] D. Lampret, OpenRISC 1200 IP Core Specification (Rev. 0.9), 2010. [Online]. Available: http://www.opencores.com
[9] J. Chen and B. C. J. Moore, "Effect of individually tailored spectral change enhancement on speech intelligibility and quality for hearing impaired listeners," in *Proc. IEEE Int. Conf. Acoust., Speech, Signal Process.*, 2013, pp. 8643–8647.
[10] J. Chen *et al.*, "Effect of enhancement of spectral changes on speech intelligibility and clarity preferences for the hearing impaired," *J. Acoust. Soc. Amer.*, vol. 131, no. 4, pp. 2987–2998, Apr. 2012.
[11] J. Chen *et al.*, "Effect of spectral change enhancement for the hearing impaired using parameter values selected with a genetic algorithm," *J. Acoust. Soc. Amer.*, vol. 133, pp. 2910–2920, 2013.
[12] B. C. J. Moore and B. R. Glasberg, "Suggested formulae for calculating auditory-filter bandwidths and excitation patterns," *J. Acoust. Soc. Amer.*, vol. 74, no. 3, pp. 750–753, Sep. 1983.
[13] W. Nogueira *et al.*, "Spectral contrast enhancement improves speech intelligibility in noise for cochlear implants," *J. Acoust. Soc. Amer.*, vol. 139, no. 2, pp. 728–739, Feb. 2016.
[14] M. Garrido *et al.*, "A pipelined FFT architecture for real-valued signals," *IEEE Trans. Circuits Syst. I, Reg. Papers*, vol. 56, no. 12, pp. 2634–2643, Dec. 2009.
[15] M. Ayinala *et al.*, "Pipelined parallel FFT architecture via folding transformation," *IEEE Trans. Very Large Scale Integr. Syst.*, vol. 20, no. 6, pp. 1068–1081, Jun. 2012.
[16] H.-M. Liu *et al.*, "A 98.6 μW acoustic signal processor for fully-implantable cochlear implants," in *Proc. Int. Symp. VLSI Des., Autom. Test*, 2016, pp. 1–4.
[17] B. S. Wilson *et al.*, "Better speech recognition with cochlear implants," *Nature*, vol. 352, no. 6332, pp. 236–238, Jul. 1991.
[18] S. Rosen, "Temporal information in speech: Acoustic, auditory and linguistic aspects," *Philos. Trans. Roy. Soc. London B, Biol. Sci.*, vol. 336, no. 1278, pp. 367–373, Jun. 1992.
[19] B. S. Wilson *et al.*, "Design and evaluation of a continuous interleaved sampling \050CIS\051 processing strategy for multichannel cochlear implants," *J. Rehabil. Res. Develop.*, vol. 30, no. 1, pp. 110–116, 1993.
[20] P.-C. Tsai *et al.*, "A hearing model to estimate Mandarin speech intelligibility for the hearing impaired patients," in *Proc. IEEE Int. Conf. Acoust., Speech, Signal Process.*, 2015, pp. 5848–5852.

[21] L.-L. Wang *et al.*, "A 191uW BPSK demodulator for data and power telemetry in biomedical implants," in *Proc. ACM Great Lakes Symp. VLSI*, 2013, pp. 119–123.

[22] C.-H. Cheng *et al.*, "A fully integrated closed-loop neuromodulation SoC with wireless power and bidirectional data telemetry for real-time human epileptic seizure control," in *Proc. Symp. VLSI Circuits. Dig. Tech. Papers*, 2017, pp. C44–C45.

[23] R. Zulinski and J. Steadman, "Class E power amplifiers and frequency multipliers with finite DC-feed inductance," *IEEE Trans. Circuits Syst.*, vol. CAS-34, no. 9, pp. 1074–1087, Sep. 1987.

[24] D. Milosevic *et al.*, "Explicit design equations for class-E power amplifiers with small DC-feed inductance," in *Proc. Eur. Conf. Circuit Theory Des.*, 2005, pp. 101–104.

[25] Z. Luo *et al.*, "A digitally dynamic power supply technique for 16-channel 12 V-tolerant stimulator realized in a 0.18-μm 1.8-V/3.3-V low-voltage CMOS process," *IEEE Trans. Biomed. Circuits Syst.*, vol. 11, no. 5, pp. 1087–1096, Oct. 2017.

[26] Y.-K. Lo *et al.*, "Bio-impedance characterization technique with implantable neural stimulator using biphasic current stimulus," in *Proc. IEEE Eng. Med. Biol. Soc.*, Aug. 2014, pp. 474–477.

[27] R. H. Walden, "Analog-to-digital converter survey and analysis," *IEEE J. Sel. Areas Commun.*, vol. 17, no. 4, pp. 539–550, Apr. 1999.

[28] W. Lu *et al.*, "Cochlear implantation in rats: A new surgical approach," *Hear. Res.*, vol. 205, no. 1/2, pp. 115–122, Jul. 2005.

[29] C. Q. Huang *et al.*, "Reduction in excitability of the auditory nerve following acute electrical stimulation at high stimulus rates: III. Capacitive versus non-capacitive coupling of the stimulating electrodes," *Hear. Res.*, vol. 116, no. 1/2, pp. 55–64, Feb. 1998.

[30] C. van den Honert and P. H. Stypulkowski, "Characterization of the electrically evoked auditory brainstem response \050ABR\051 in cats and humans," *Hear. Res.*, vol. 21, pp. 109–126, 1986.

[31] J. T. McElveen *et al.*, "Effect of mastoid cavity modification on middle ear sound transmission," *Ann. Otol. Rhinol. Laryngol.*, vol. 91, no. 5, pp. 526–532, Sep. 1982.